A MINIATURE FLYWHEEL ENERGY STORAGE SYSTEM SUPPORTED BY HYBRID MAGNETIC BEARINGS WITH H^{∞} CONTROLLER

Mochimitsu Komori
Kyushu Institute of Technology, Iizuka, Fukuoka 820 JAPAN
Nobuyki Akinaga
Kyushu Institute of Technology, Iizuka, Fukuoka 820 JAPAN
Hideki Sakai
Kyushu Institute of Technology, Iizuka, Fukuoka 820 JAPAN

ABSTRACT

This paper discusses a prototype of miniature flywheel energy storage system. The system consists of a rotor with a flywheel disk and a pair of hybrid magnetic bearings (HMBs). The HMB is composed of both superconducting magnetic bearings (SMBs) and active magnetic bearings (AMBs). The rotor measures 270 mm in length and 24 mm in diameter with a flywheel disk (100 mm in diameter). The rotor mass with the flywheel is 1.2 kg, which is supported by the repulsive force between two permanent magnets (PMs). The rotor model is represented by second-order functions. H-infinity control method and zero bias method are applied to the AMB. In this paper, the design and dynamics of the flywheel energy storage system are discussed. The H-infinity controller is successfully applied to the system. The experimental results show that by using the HMBs the displacement of the rotor is much smaller than that with SMBs, that the HMBs suppress both radial and axial displacements, and that the H infinity control is applicable to the storage system.

INTRODUCTION

Recently, consuming energy effectively and usefully is very important for energy saving and our future life. Thus, energy-saving technology for surplus power is very important. A flywheel energy storage system is one of the valuable energy-saving technologies. The system is very simple and characterized by high energy saving compared with other energy storage system.

On the other hand, high temperature superconductors having strong pinning force are useful for industrial applications. There are many reports on application systems based on large pinning force [1-3]. Our group has been studying hybrid magnetic bearings (HMBs) composed of both superconducting magnetic bearings (SMBs) and active magnetic bearings (AMBs).

In this paper, we propose a miniature flywheel energy storage system. The HMBs with H-infinity control method are applied to the flywheel energy storage system. The dynamics of the energy storage system is discussed. Especially, the dynamics using HMBs and SMBs in a vacuum are studied compared with that in the air.

SYSTEM

Structure

We have developed a prototype of miniature flywheel energy storage system. The system consists of a rotor

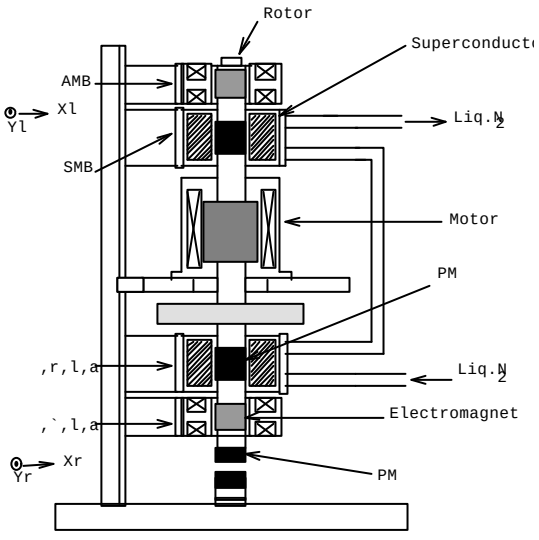

FIGURE 1: Schematic illustration of the fly-wheel energy storage system

with a flywheel disk and a pair of HMBs. The rotor measures 270 mm in length and 24 mm in diameter with a flywheel disk (100 mm in diameter). The rotor mass with the flywheel is 1.2 kg, which is supported by the repulsive force between two permanent magnets (PMs). In our system, the SMBs are more dominant than the AMBs. This means that the AMBs assist the SMBs. In order to suppress the rotor vibration near the resonance rotation speed, H-infinity control is applied to the AMB. Except near the resonance rotation speed, the SMB mainly suppress the rotor vibration. The superconductors of the SMBs were field-cooled. The energy storage system is characterized by the HMB, H-infinity control, and the repulsive force between the PMs. Moreover, the controller without bias currents is applied to the AMBs.

In our energy storage system, the SMBs are considered to be dominant for suppressing the rotor displacement. Thus, a nonlinear control method without bias currents is adopted to the system. In the rotor control, both of the electromagnets facing each other aren't excited by the driving currents at the same time. That is, the driving current is applied to one of the electromagnets facing each other.

SYSTEM

Model

In order to make the rotor model with SMBs, we measured the compliance of the rotor supported by the SMBs. Figure 2 shows the compliance of the rotor with SMBs. In the figure, the solid and dotted lines represent experimental and theoretical results, respectively. We applied the 2nd order models to the experimental result, which are given by

$$m\ddot{x}_G + c\dot{x}_G + kx_G = f_{xL} + f_{xR} + f_{xd}\,, \qquad (1)$$

$$J\ddot{q} + c_r\dot{q} + k_r q = -\ell_b f_{xL} + \ell_b f_{xR} + m_{qd}\,, \qquad (2)$$

$$m\ddot{y}_G + c\dot{y}_G + ky_G = f_{yL} + f_{yR} + f_{yd}\,, \qquad (3)$$

$$J\ddot{f} + c_r\dot{f} + k_r f = \ell_b f_{yL} - \ell_b f_{yR} + m_{fd}\,, \qquad (4)$$

where x_G and y_G are displacements of the rotor, f_{ij} $(i = x, y,\ \ j = L, R)$ are attractive forces to the rotor, f_{id} $(i = x, y)$ are disturbances for the rotor, q and f are rotation angles of the rotor, m_{ld} $(l = q, f)$ are moments of the rotor. From Figure 2, it is found that the measured compliance almost equal to the theoretical compliance. This shows that dynamic models for the rotor with SMBs are represented by the 2nd order functions.

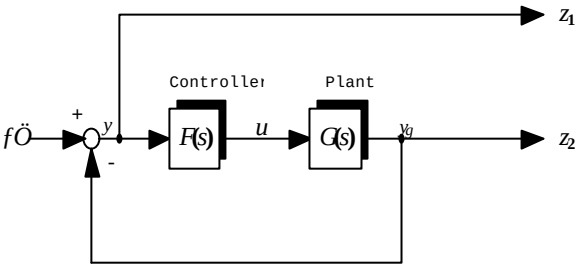

FIGURE 3: Block digram of a feedback control system

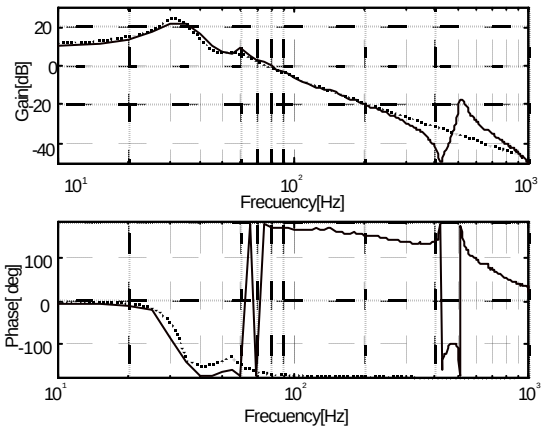

FIGURE 2: Compliance of the rotor supported by the SMBs

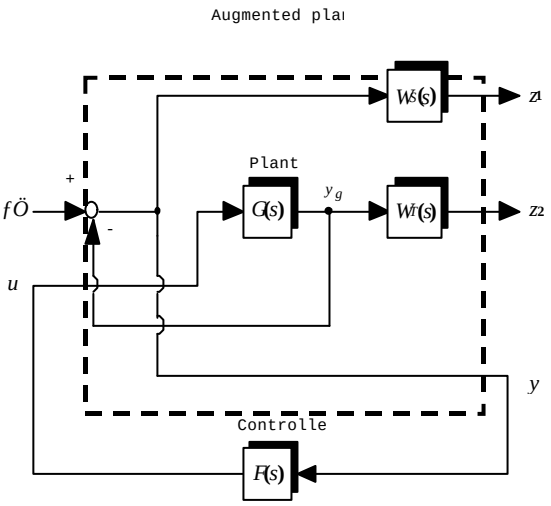

FIGURE 4: Feedback control system with augmented plant

H^{∞} controller design

Now, we consider a feedback control system as shown in Figure 3, where $F(s)$ is a controller, $G(s)$ is a plant, w, u, y_g, z_1, z_2 are variables. According to the H infinity theory, the sensitivity function $S(s)$ is defined as a transfer function from w to y, and the complementary sensitivity function $T(s)$ is defined as a transfer function from w to y_g. These transfer functions are represented by

$$S(s) = \frac{1}{1+L(s)} \tag{5}$$

$$T(s) = \frac{L(s)}{1+L(s)} \tag{6}$$

where

$$L(s) = G(s)F(s) \tag{7}$$

Since neither the function $S(s)$ nor the function $T(s)$ becomes small, weighting functions $W_S(s)$ and $W_T(s)$ are introduced to the system in Figure 3. The functions $W_S(s)$ and $W_T(s)$ are the sensitivity function and the complementary sensitivity function, respectively. Then, we transform Figure 3 to Figure 4 using the functions $W_S(s)$ and $W_T(s)$. Figure 4 shows a feedback control system with augmented plant. In this paper, we applied our energy storage system to the augmented plant. The H infinity controller is designed as a mixed sensitivity problem so that the controller satisfies Eq. (8).

$$\left\| \begin{matrix} W_S(s)S(s) \\ W_T(s)T(s) \end{matrix} \right\|_{\infty} < 1 \tag{8}$$

Since the compliance in Figure 2 is found to be large in the low frequency range, the system needs larger weighting function $W_S(s)$ in this range. Especially, the weighting function $W_S(s)$ should be large near the resonance frequency. The weighting function $W_T(s)$ becomes small in the low frequency range and large in the high frequency range. As a result, we adopted these weighting function given in Eqs. (9) and (10).

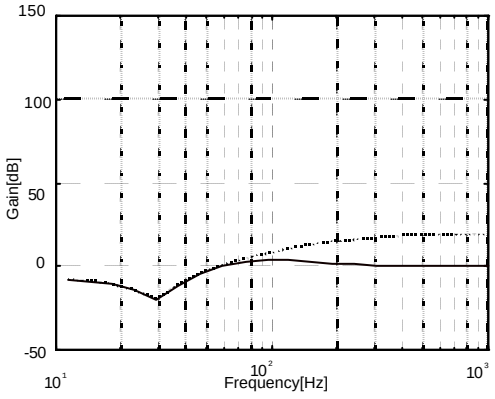

FIGURE 5: Bode plots of the sensitivity function $S(s)$ and the inverse weighting function $1/W_S(s)$

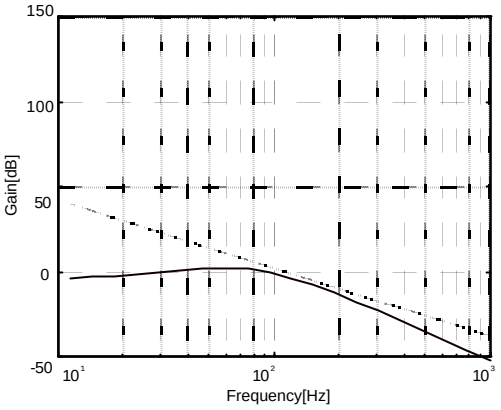

FIGURE 6: Bode plots of the complementary sensitivity function $T(s)$ and the inverse weighting function $1/W_T(s)$

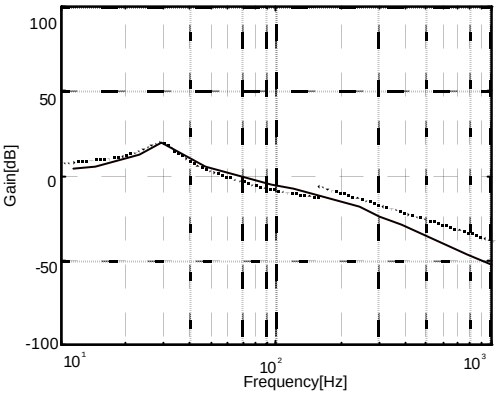

FIGURE 7: Bode plots of designed open loop transfer function

$$W_S(s) = \frac{0.1667s^2 + 742.9286s + 260000}{4.0000s^2 + 282.0000s + 450000} \tag{9}$$

$$W_T(s) = \frac{s^2}{5000000} \tag{10}$$

Figure 5 shows the sensitivity function $S(s)$ and its inverse weighting function $1/W_S(s)$. The function $S(s)$ is entirely equal to the function $1/W_S(s)$ in the low frequency range. The complementary sensitivity function $W_T(s)$ and its inverse weighting function $1/W_T(s)$ are shown in Figure 6. The functions $S(s)$ and $1/W_S(s)$ are almost equal to each other in the high frequency range. These show that weighting functions $W_S(s)$ and $W_T(s)$ are well set up for the functions $S(s)$ and $T(s)$, respectively. Figure 7 shows the

designed open loop transfer function, the sensitivity function $W_S(s)$, and the inverse weighting function $1/W_T(s)$. From Figure 7, the close loop transfer function is found to be well shaped by the functions $W_S(s)$ and $1/W_T(s)$. In the loop shaping process, the gain margin and the phase margin become between 3-10 dB and over 20 deg, respectively.

The H infinity controller gives control signals to the system. In the experiments, we use zero bias metod on the AMBs. Fundamentary, the method is based on a root method. The final output to amplifier is given by

$$V_{ij} = sign\left(f_{i_j}\right)\frac{1}{k_a\sqrt{k}}\sqrt{\left|f_{ij}\right|}\left\{\ell_a - sign\left(f_{ij}\right)w_i\right\}, \quad (11)$$

where

$$sign\left(f_{ij}\right) = \begin{cases} 1, & f_{ij} > 0 \\ 0, & f_{ij} = 0 \\ -1, & f_{ij} < 0 \end{cases} \quad (12)$$

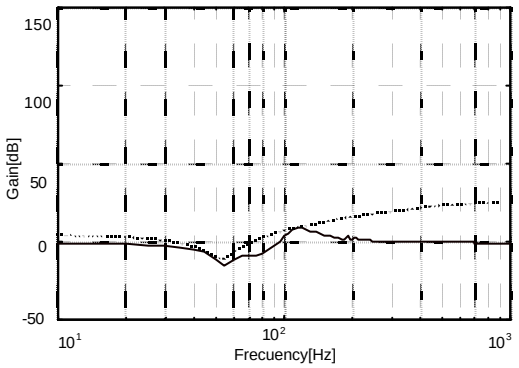

FIGURE 8: Bode plots of the experimental sensitivity function $S(s)$ and the inverse weighting function $1/W_S(s)$

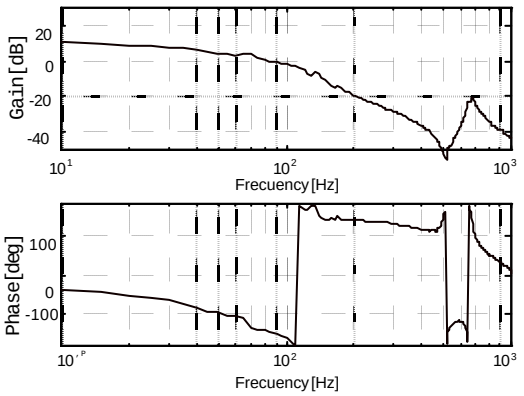

FIGURE 9: Compliance of the rotor supported by the HMB with H infinity controller

EXPERIMENTS AND DISCUSSIONS

Frequency response

Before going into the rotation dynamics, we measured the sensitivity function $S(s)$ and the complementary sensitivity function $T(s)$ experimentally. Figure 8 shows the experimental sensitivity function (solid line) and the inverse weighting function $1/W_S(s)$ (dotted line). The function $1/W_S(s)$ is above the sensitivity function $S(s)$ over the entire frequency range. This means that the designed controller satisfies Eq. (8). The complementary sensitivity function $T(s)$ is also

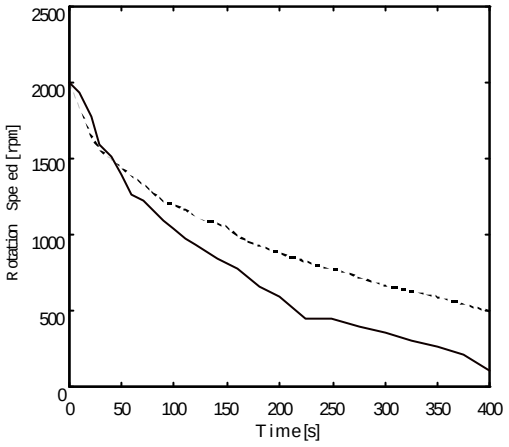

FIGURE 10: Rotation decay characteristics for the rotors with SMBs (dotted line) and HMBs (solid line) in the air

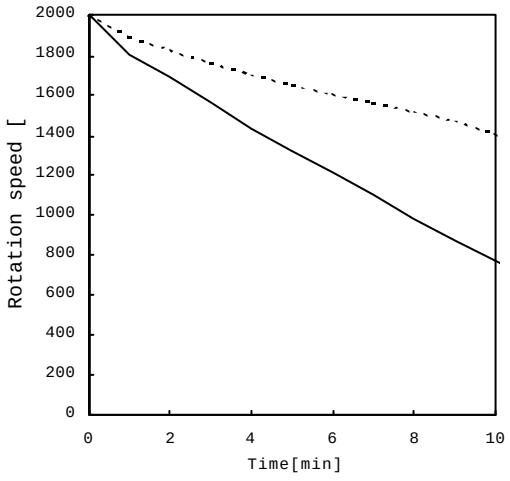

FIGURE 11: Rotation decay characteristics for the rotors with SMBs (dotted line) and HMBs (solid line) in the vacuum

measured experimentally. As a result, it is found that the function $T(s)$ satisfies Eq. (8) as well as the sensitivity function $S(s)$.
When the H infinity controller designed here is applied to the system, the compliance is measured experimentally as shown in Figure 9. The compliance in Figure 9 is improved better than that in Figure 2. Especially near the resonance frequency, there is no compliance peak in Figure 9.

Rotation dynamics
First, we investigated the effect of air resistance on the rotation speed. In the experiment, the natural rotation decays for the rotor with HMBs and SMBs were investigated. Figures 10 and 11 show the results in the air and the vacuum ($<$ 50 Pa), respectively. In each figure, the solid and dotted lines correspond to the results for the HMBs and the SMBs, respectively. From Figures 10 and 11, the rotation speed for the rotor with HMBs decreases more than the rotor with SMBs in the air and the vacuum. The rotation speed for the rotor in the air decreases more than that of the rotor in the vacuum. The decay time in the air (Figure 10) is about 3-5 times as short as that in the vacuum (Figure 11). This is caused by the air resistance. This result indicates that air resistance is very effective on the rotation speed decays. The vacuum pressure 50 Pa is so high compared with the air pressure $\approx$1000 hPa in order to investigate the effect of the air resistance.
Next, the rotor displacement was measured during the rotation decay. Figure 12 shows the relationship between the radial displacement and the rotation speed for the rotor with SMBs in the vacuum. The displacement is about 0.1 mm over the entire speed range. The relationship between the radial displacement and the rotation speed for the rotor with HMBs in the vacuum is shown in Figure 13. The displacement in Figure 13 is about 0.05 mm over the entire speed range. The displacement for the rotor with HMBs (Figure 13) is half as much as that with SMBs (Figure 12). This shows that the energy storage system with HMBs is more useful than the system with SMBs in suppressing the radial displacement.
We have estimated energy loss for the systems with HMBs in the vacuum and in the air. The energy loss is estimated by calculating the rotation speed decays of the rotor in the vacuum and the air. The result is shown in Figure 14, where the solid and dotted lines correspond to the results in the vacuum and the air. The result shows that the energy loss in the air as well as the loss in the vacuum becomes larger with increasing rotation speed. The difference between the two losses is caused by the air resistance.
Figure 15 shows the relationship between the energy

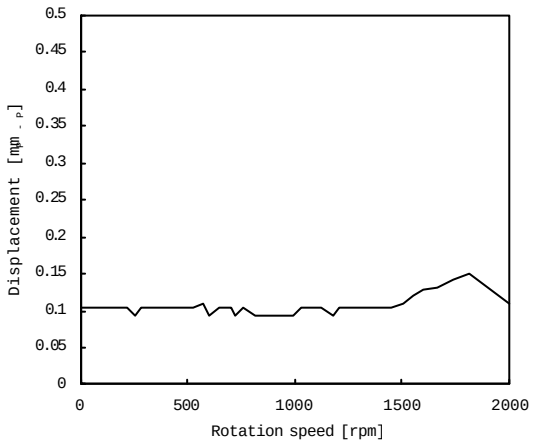

FIGURE 12: Relationship between the radial displacement and the rotattion speed for the rotor with SMBs.

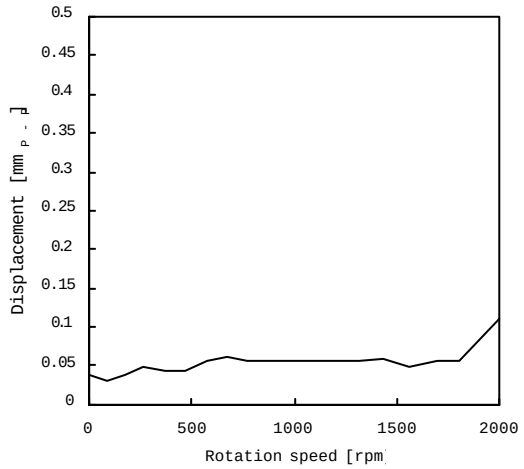

FIGURE 13: Relationship between the radial displacement and the rotattion speed for the rotor with HMBs.

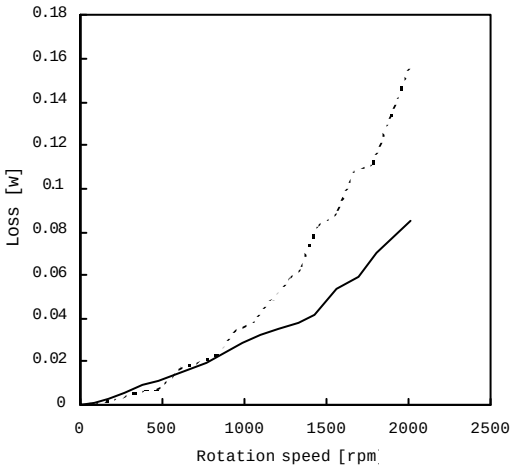

FIGURE 14: Relationship between the energy loss and the rotation speed in the vacuum (solid line) and in the air (dotted line).

loss and the rotation speed in the vacuum. The solid and dotted lines correspond to the systems with HMBs and SMBs. The energy loss is estimated by calculating the rotation speed decay of the rotor. The energy losses for the two cases become larger as the rotation speed increases. However, the loss for the system with SMBs is much larger than that with HMBs. This is because the vibration of the rotor with HMBs is smaller than that with SMBs in both radial and axial directions. As a result, the system with HMBs is better than that with SMBs.

CONCLUSION

We have developed a prototype of miniature flywheel energy storage system. The system consists of a rotor with a flywheel disk and a pair of HMBs (SMBs + AMBs). H-infinity controller is successfully applied to the system. The experimental results show that by using the HMBs the radial displacement of the rotor is much smaller than that with SMBs. Moreover, the HMBs suppress both radial and axial displacements. This shows that the system with HMBs is effective on suppressing the axial and radial displacements. The energy loss in the air as well as in the vacuum becomes larger with increasing rotation speed. The loss for the system with SMBs is much larger than that with HMBs. This is because the vibration of the rotor with HMBs is smaller than that with SMBs in both radial and axial directions. As a result, the system with HMBs is better than that with SMBs.

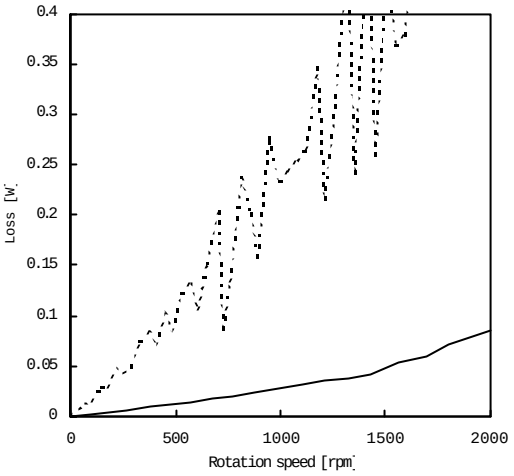

FIGURE 15: Relationship between the energy loss and the rotation speed. The solid and dotted lines correspond to the systems with HMBs and SMBs.

REFERENCES

1. J.R.Hull, and et al., Low rotational drag in high-temperature superconducting bearings," IEEE Trans. Appl. Supercond., vol.5, 1995.
2. H.J.Borneman and M.Sander, Conceptual system design of a 5 MWh/100 MW superconducting flywheel energy storage plant for power utility applications, IEEE Trans. Appl. Supercond., vol.7, 1997.
3. M.Komori, and et al., A hybrid-type superconducting magnetic bearing system with nonlinear control, IEEE Trans. Appl. Supercond., vol.8, 1998.